

A novel image fusion algorithm based on nonsubsampling shearlet transform and morphological component analysis

Xingbin Liu¹ · Wenbo Mei¹ · Huiqian Du¹ · Jiadi Bei¹

Received: 22 March 2015 / Revised: 22 August 2015 / Accepted: 14 November 2015 / Published online: 25 November 2015
© Springer-Verlag London 2015

Abstract We propose a novel image fusion algorithm which involves nonsubsampling shearlet transform (NSST) and morphological component analysis (MCA). The source images are decomposed into several subbands of different scales and directions by NSST. MCA is performed on the low-pass subbands to extract more salient features, and then, the separated cartoon parts and texture parts are fused, respectively. The larger high-pass subbands coefficients are selected by sum-modified-Laplacian scheme in order to obtain more useful information from the source images. The final fused image can be reconstructed by performing inverse NSST on the fused subbands. Experiments on different kinds of images verify the effectiveness of the proposed algorithm, and experimental results show that the proposed algorithm outperforms other methods in both the visual effect and objective evaluation.

Keywords Image fusion · Multi-scale transform · Nonsubsampling shearlet transform · Morphological component analysis

1 Introduction

With the rapid development of sensor technology, the same scene can be captured by multiple imaging sensors. In order to take advantages of the diverse features of multimodal images, image fusion techniques are applied to combine images obtained from multiple sensors to form a new single one, which can provide enhanced representation for visual perception and is also suitable for computer processing.

Over the past few decades, various image fusion algorithms have been proposed [1–6]. As one very important and widely used category, the multi-resolution analysis (MRA)-based image fusion algorithms improve the fusion effect by performing fusion process in different scales. The development of the MRA-based image fusion algorithms has gone through three stages, including pyramid transform [7,8], wavelet transform [9–11] and multi-scale geometric analysis (MGA) [12–16]. As the wavelet transform coefficients present directionality, the fusion methods based on wavelet transform can achieve better fusion effect than those based on pyramid transform. Wavelet transform are good at catching point singularities, but lack the ability of representing multi-dimensional features, such as contours and edges. Therefore, the fusion methods with wavelet transform will inevitably cause blur in the edges and details, which are the most important information of images. Based on the theory of wavelet transform, an MGA tool called ridgelet transform is built [17], which is more suitable to represent anisotropy features and achieves good fusion results [18]. Subsequently, curvelet and contourlet transform are used in image fusion [19,20]. As contourlet transform has good anisotropic directional selectivity, it can obtain good fusion effect, but lead to pseudo-Gibbs phenomenon due to subsampling operation. To overcome this shortcoming,

✉ Huiqian Du
duhuiqian@bit.edu.cn

Xingbin Liu
xbliu6@163.com

Wenbo Mei
wbmei@bit.edu.cn

Jiadi Bei
beijiadi@126.com

¹ School of Information and Electronics, Beijing Institute of Technology, Beijing 100081, China

the nonsubsamped contourlet transform (NSCT) with shift-invariance is introduced to the field of image fusion [12], which suppresses the pseudo-Gibbs phenomenon, but the computation is heavy. As a new MGA tool, the shearlet transform [21] provides a way to represent image sparsely. Shi et al. use shear filter to decompose source images in the application of remote sensing image fusion and achieve good fusion result [22]. The nonsubsamped shearlet transform (NSST) [23] inherits the advantages of shearlet transform and adds the property of shift-invariant. Compared to the NSCT, the NSST has higher computational efficiency and stronger selectivity of anisotropic direction. Therefore, the NSST has been widely applied in various applications of image fusion, such as visible light and infrared image fusion [24], medical image fusion [25] and multi-focus image fusion [26].

For the MGA-based image fusion methods, the core problems include choosing the MGA transform and designing fusion rules. Generally, it is easy to extract features from high-pass subbands as their representations approximate sparse. However, for the low-pass subband, the most adopted fusion rule is the ‘averaging’ scheme. Since the low-pass subband contains main energy and still includes some details of the image, the traditional averaging scheme will lead to reduction in the contrast and loss of some important information. The low-pass subband of NSST combined with appropriate fusion rules have achieved some satisfactory fusion results. Liu et al. proposed a fusion rule based on regional energy to fuse low-pass subbands decomposed by NSST [27]. Kong utilizes the model of region average energy to fuse low-pass subband of NSST domain [28]. These methods process the low-pass subband as a whole and neglect the morphological features existed in the low-pass subband. Morphological component analysis (MCA) [29] can morphologically decompose an image into cartoon part and texture part by sparse representation. As the features of approximation image can be extracted by MCA, the MCA can be employed in the fusion of low-pass subbands.

According to the above analysis, we propose a novel image fusion algorithm based on NSST and MCA. The source images are decomposed by NSST to obtain the low-pass approximation subbands and a series of sparse approximate high-pass subbands. For the obtained low-pass subbands, the cartoon parts and texture parts separated by MCA are fused, respectively, to obtain the fused low-pass subband. The fusion rule of high-pass subbands is the sum-modified-Laplacian (SML) scheme. Finally, the inverse NSST is applied on the fused subbands to reconstruct the final image. Experimental results demonstrate that the proposed method can preserve more detail information in the fused image.

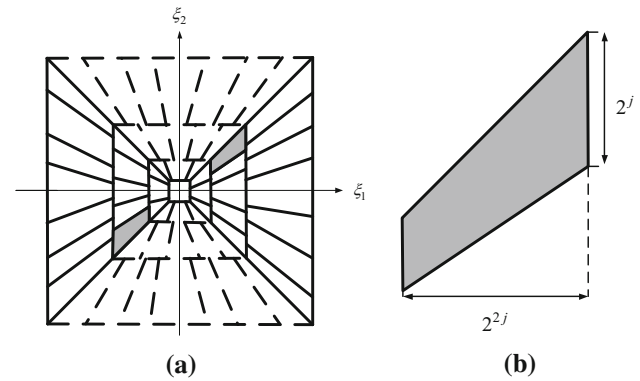


Fig. 1 The structure of the frequency partition by NSST. **a** The frequency plane, **b** the frequency support of shearlet

2 Basic theory

2.1 Nonsubsamped shearlet transform

The NSST is a state-of-the-art MGA tool, which has the features of shift-invariance and excellent anisotropic direction selectivity [23]. The implementation procedures of the NSST include multi-scale partition and direction localization. Non-subsampled Laplacian pyramid filter is introduced to the multi-scale partition process, which ensures the property of shift-invariance and therefore suppresses the pseudo-Gibbs phenomenon in the fused image. The process of direction localization can provide more directional details information, which is realized by shift-invariant shearing filters banks. After transformed by NSST, the image can be decomposed into one low-pass subband and a series of high-pass subbands, and all the subbands have the same size as the original image. The frequency support of shearlet is a pair of trapezoids, the size of which is $2^{2j} \times 2^j$, and the frequency partition of NSST is shown in Fig. 1.

2.2 Morphological component analysis

MCA [29] can successfully separate an image into different morphological features based on sparse representation, which can be applied for decomposing an image into texture part and cartoon part. Suppose an image x can be linear combined by K parts,

$$x = \sum_{k=1}^K x_k \quad (1)$$

where each component x_k represents a morphologically different part. MCA relies on the assumption that x_k can be sparsely represented by a given dictionary Φ_k ; i.e.,

$$x_k = \Phi_k \alpha_k \quad (2)$$

Fig. 2 The MCA decomposition results. **a** Original Barbara image, **b** the cartoon part of Barbara, **c** the texture part of Barbara



but other dictionaries $\Phi_{l \neq k}$ cannot sparsely represent x_k , where α_k denotes the coefficient of sparse representation.

To decompose an image into texture part and cartoon part, the following problem needs to be solved,

$$\begin{aligned} \{\alpha_T^{\text{opt}}, \alpha_C^{\text{opt}}\} &= \arg \min_{\{\alpha_T, \alpha_C\}} \|\alpha_T\|_0 + \|\alpha_C\|_0, \\ \text{s.t. } x &= \Phi_T \alpha_T + \Phi_C \alpha_C \end{aligned} \quad (3)$$

where Φ_T and Φ_C , respectively, represent the dictionaries chosen for the text part and cartoon part, α_T and α_C , respectively, denote corresponding representation coefficients of text part and cartoon part. The problem described in Eq. (3) is hard to solve as it is nonconvex. Therefore, an approximation problem is formed by relaxing the constraint,

$$\begin{aligned} \{\alpha_T^{\text{opt}}, \alpha_C^{\text{opt}}\} &= \arg \min_{\{\alpha_T, \alpha_C\}} \{\|\alpha_T\|_1 + \|\alpha_C\|_1 \\ &\quad + \lambda \|x - \Phi_T \alpha_T - \Phi_C \alpha_C\|_2^2\} \end{aligned} \quad (4)$$

Equation (4) can be efficiently solved by the block coordinate relaxation (BCR) algorithm [30]. Figure 2 illustrates the decomposition results of the Barbara image.

3 Image fusion algorithm based on NSST and MCA

Suppose two source images A and B are desired to be fused, we assume A and B have been geometrically registered in advance and the final fused image is denoted as F . The general fusion procedure of the proposed scheme can be elaborated as follows:

Step 1 Decompose two source images into two low-pass subbands $\{A_0, B_0\}$ and a series of high-pass subbands $\{A_{j,r}\}, \{B_{j,r}\}$ by J -level NSST decomposition, (j, r) represent the r direction in the j -th scale.

Step 2 Separate the cartoon parts and texture parts from low-pass subbands by MCA and then obtain two pairs of

image $(A_{C0}, A_{T0}), (B_{C0}, B_{T0})$, where A_{C0} and A_{T0} denote the cartoon part and texture part of low-pass subband A_0 , B_{C0} and B_{T0} denote the cartoon part and texture part of low-pass subband B_0 .

Step 3 Fuse the cartoon parts (A_{C0}, B_{C0}) and texture parts (A_{T0}, B_{T0}) , respectively, to obtain the fused cartoon part F_{C0} and fused texture part F_{T0} . Then, the fused low-pass subband F_0 can be obtained by merging fused cartoon part F_{C0} and fused texture part F_{T0} .

Step 4 Fuse the high-pass subbands $\{A_{j,r}\}$ and $\{B_{j,r}\}$ by using the sum-modified-Laplacian (SML) scheme.

Step 5 Apply the inverse NSST to the combined subbands to reconstruct the fused image F .

The scheme described above is the overall framework and detailed realization of the fusion algorithm will be given in the following section. The schematic diagram of the proposed image fusion algorithm is shown in Fig. 3.

3.1 Low-pass subband fusion

The low-pass subbands are the approximation of source images, which contain the main energy. The simple averaging fusion rule used to integrate the low-pass subbands directly in most fusion algorithms will lead to reduction in the fused image contrast and loss of useful information. In order to utilize the morphological diversity of low-pass subbands, the MCA is applied in the fusion of low-pass subbands.

According to the theory of MCA, the obtained low-pass subbands can be decomposed into the cartoon parts and texture parts based on sparse representation. The sparse representation coefficients can express salient features, inherent characteristics and structures of the source images. Therefore, the activity level is measured by the absolute value of sparse representation coefficients. The larger the absolute value of coefficient, the more information it contains. For transferring more information to the fused image, the maximum fusion rule is chosen in the fusion scheme,

$$\alpha_F = \begin{cases} \alpha_A & \text{if } |\alpha_A| \geq |\alpha_B| \\ \alpha_B & \text{otherwise} \end{cases} \quad (5)$$

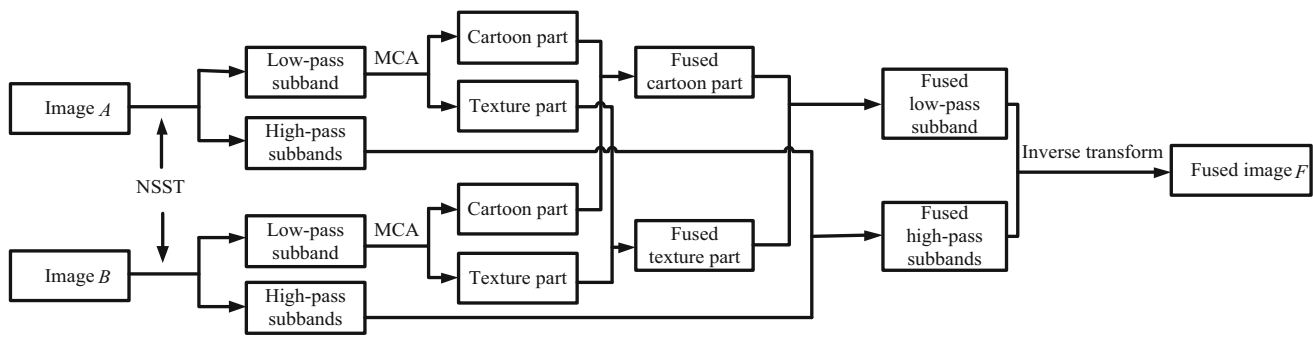


Fig. 3 Schematic diagram of image fusion algorithm based on NSST and MCA

$$\beta_F = \begin{cases} \beta_A & \text{if } |\beta_A| \geq |\beta_B| \\ \beta_B & \text{otherwise} \end{cases} \quad (6)$$

where α_A and α_B denote cartoon part coefficients of image A and image B , respectively. The β_A and β_B represent texture part coefficients of image A and image B , and the fused sparse coefficients of cartoon part and texture part denote as α_F and β_F , respectively.

3.2 High-pass subbands fusion

The directional high-pass subbands mainly include the detail information, such as edges and linear features. Since the sum-modified-Laplacian (SML) [31] can well reflect the significance of the image features, therefore, the SML scheme is chosen for the fusion of directional high-pass subbands. The SML is defined as follows:

$$\text{SML}(m, n) = \sum_{p=-P}^P \sum_{q=-Q}^Q \text{ML}(m+p, n+q) \quad (7)$$

$$\begin{aligned} \text{ML}(m, n) = & |2H(m, n) - H(m+step, n) \\ & - H(m-step, n)| + |2H(m, n) \\ & - H(m, n+step) - H(m, n-step)| \end{aligned} \quad (8)$$

where $H(m, n)$ denotes the coefficient of one subband in the position (m, n) , $step$ is the measure distance of coefficients. The SML is measured in a square-shaped window, and the parameters P and Q determine the size of the measure window. In this paper, window size is 3×3 and $step$ equals 1. The specific fusion rule for high-pass subbands is defined as follows:

$$H_F^{l,k}(m, n) = \begin{cases} H_A^{l,k}(m, n) & \text{if } \text{SML}_A^{l,k}(m, n) \geq \text{SML}_B^{l,k}(m, n) \\ H_B^{l,k}(m, n) & \text{otherwise} \end{cases} \quad (9)$$

where $\text{SML}_A^{l,k}(m, n)$ and $\text{SML}_B^{l,k}(m, n)$ denote the SML value of the l -scale and k -directional subband in the position (m, n) of image A and image B , respectively. The

$H_A^{l,k}(m, n)$, $H_B^{l,k}(m, n)$ and $H_F^{l,k}(m, n)$ denote the coefficients of image A , image B and the fused image F in the position (m, n) , respectively.

4 Experimental results and discussion

To verify and evaluate the performance of the proposed image fusion scheme, experiments were performed on several images pairs, including multi-focus images, medical images, infrared and visible images. In order to demonstrate the validity of the proposed image fusion method, the proposed method is compared with five widely used methods based on multi-resolution analysis tools, which are gradient pyramid (GP)-based method [8], discrete wavelet transform (DWT)-based method [9], nonsubsampled Contourlet transform (NSCT)-based method [32], nonsubsampled shearlet transform (NSST)-based method [33] and morphological component analysis (MCA)-based method [6]. In the experiments, the decomposition layer number for all the methods is 4. The DBSS (2, 2) wavelet is chosen for the images fused by DWT-based method. The directions of NSCT and NSST are (4, 4, 8, 8) from coarser to finer scales. The pyramid filter used in the NSCT is ‘9–7,’ and the directional filter is ‘pkva.’ In the NSST, ‘maxflat’ is used as the pyramid filter. The dictionaries chosen for the cartoon parts and the texture parts are curvelet and local DCT, respectively. In all these compared methods, the fusion rule adopted in the low-pass subbands is ‘averaging’ rule and the high-pass subbands are merged by ‘absolute maximum choosing’ rule.

Apart from subjective visual appearance observation, universal image quality index Q_0 [34], weighted fusion quality index Q_W [35], edge-dependent fusion quality index Q_E [35], normalized weighted performance metric $Q^{AB/F}$ [36] and entropy are introduced to evaluate the quality of the fused images objectively. The Q_0 measures structural distortions of the fused image. The Q_W and Q_E are defined based on Q_0 , which are effective in measuring the salient information of source images transferred to the fused image. The $Q^{AB/F}$ metric measures the edge information transferred

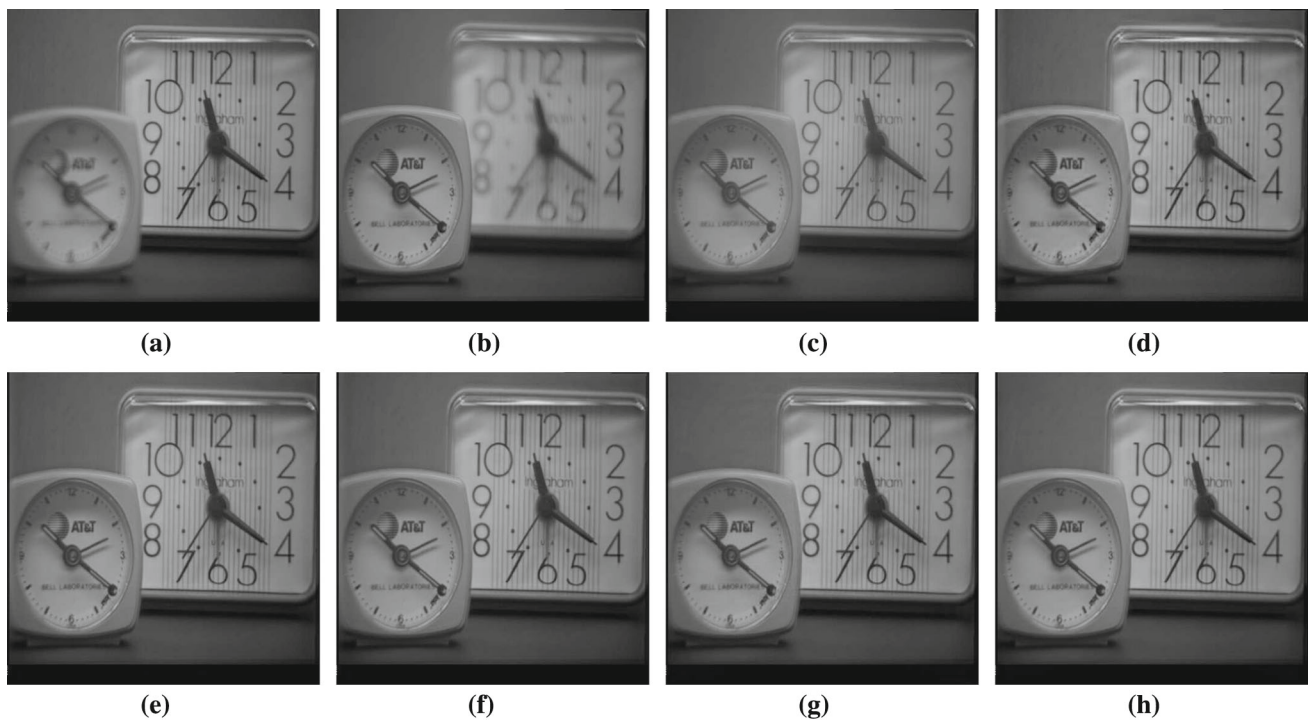


Fig. 4 Multi-focus images and the corresponding fused images. **a** Right-focused image, **b** left-focused image, **c** GP, **d** DWT, **e** NSCT, **f** NSST, **g** MCA, **h** NSST + MCA

from source image to the fused image. The entropy can reflect the amount of information contained in the fused image. The larger values of the metrics described above mean that the quality of the fused image is better. The best numerical results are marked with bold font in the following tables.

4.1 Fusion of multi-focus images

Due to the limited field depth of optical imaging systems, it cannot assure all the relevant objects in the captured images are in focus. Generally, the objects in focus appear sharp, while the objects out of focus blur. Therefore, fuse multi-focus images to obtain a clear image that every object in focus is important and useful in the applications like target recognition and machine perception. The experimental results of different methods performing on multi-focus images are shown in Fig. 4. Figure 4a, b is two perfectly registered multi-focus images; the right area of Fig. 4a is in focus, while the left area of Fig. 4b is in focus. Figure 4c–h shows the fused images with five compared methods mentioned above. By carefully observing the fused images, Fig. 4c is of low contrast and looks fuzzy and Fig. 4d–g introduces varying degrees of ripples and artifacts in the edge positions. Figure 4h fused by the proposed method effectively suppresses the blur in the edges and achieves the best visual effect. The quantitative results of objective evaluation metrics are given in Table 1, and the proposed image fusion algorithm outperforms other

Table 1 Quantitative comparison results of the fused multi-focus images

Methods	Q_E	Q_W	Q_0	$Q^{AB/F}$	Entropy
GP	0.4628	0.8865	0.7609	0.6395	7.0580
DWT	0.5017	0.9116	0.7350	0.6284	7.0575
NSCT	0.5339	0.9227	0.7728	0.6672	7.0451
NSST	0.5350	0.9226	0.7736	0.6685	7.0457
MCA	0.4988	0.9207	0.7434	0.6285	7.0781
Proposed	0.5623	0.9221	0.7749	0.6777	7.0895

compared methods in four of the five metrics, i.e., Q_E , Q_0 , $Q^{AB/F}$ and entropy.

4.2 Fusion of medical images

With the development of medical imaging techniques, such as magnetic resonance imaging (MRI), computed tomography (CT), single photon emission computed tomography (SPECT) and so on, different imaging techniques capture the different information of human tissues. Combining the multi-modality medical images into single one is helpful for medical analysis and diagnose. For instance, CT image shows bones clearly, while the MRI image can provide more detailed information of soft tissues. The fused image can retain both the bones detail and soft tissues information. In

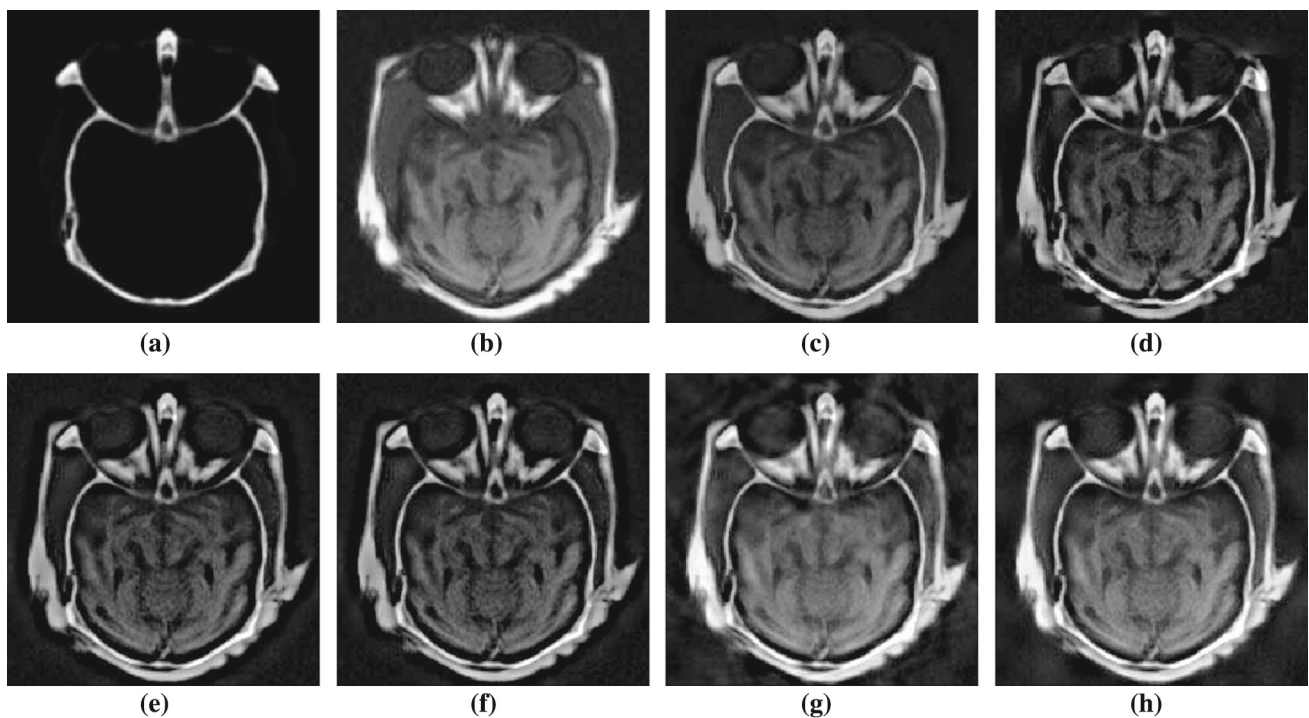


Fig. 5 Medical images and the corresponding fused images. **a** CT image, **b** MRI image, **c** GP, **d** DWT, **e** NSCT, **f** NSST, **g** MCA, **h** NSST + MCA

Table 2 Quantitative comparison results of the fused medical images

Methods	Q_E	Q_W	Q_0	$Q^{AB/F}$	Entropy
GP	0.5043	0.7465	0.6527	0.6807	6.3104
DWT	0.4290	0.7397	0.5915	0.6166	6.1512
NSCT	0.4761	0.7726	0.6145	0.6920	6.1488
NSST	0.4688	0.7717	0.6115	0.6877	6.1705
MCA	0.4240	0.8417	0.5943	0.6393	7.0632
Proposed	0.5490	0.8592	0.7342	0.7351	7.0394

the experiment, two registered CT and MRI images are shown in Fig. 5a, b and the fused images with compared methods are shown in Fig. 5c–h. It can be seen from the fused images, the center parts of Fig. 5c–f are darker than the original MRI image, while the pixels in Fig. 5g, h retain the consistent intensity as the original MRI image. However, the contrast in the lower right part of Fig. 5g is not so obvious as that of Fig. 5h. The quantitative results of objective evaluation metrics are given in Table 2, which indicate that the proposed image fusion algorithm achieves the best results in the listed evaluation metrics except entropy.

4.3 Fusion of infrared and visible images

The spectral bands of infrared and visible images are different. The infrared image can well capture features of the thermal object, while the visible image can depict spatial

details. The complementary features of the infrared and visible images can be displayed in the fused image. Figure 6a, b depicts a pair of infrared and visible images, and the fused images by compared methods and our proposed method are shown in Fig. 6c–h. It can be noted that Fig. 6c loses some useful detail information, and Fig. 6d–g is of low contrast. In addition, Fig. 6d introduces some discontinuity in the road and some artifacts exist in Fig. 6g. As revealed in Fig. 6h, the clarity of the image fused by the proposed method is higher and the contrast is reasonable. Table 3 provides the quantitative results of objective evaluation metrics, and it can be seen that the proposed image fusion algorithm achieves the best results in the metrics Q_E , Q_W , Q_0 and entropy.

4.4 Further analysis and discussion

The above experiments verify that the proposed scheme is effectively suitable for multi-focus image fusion and several kinds of multi-sensor image fusion. It can be seen from the experimental results that the fused images by using the proposed method preserve more detail information than the images fused by other methods. The higher objective values of metrics mean that more details are transferred to the fused image, and the objective evaluation coincides with the visual effect. Particularly, it can be seen from the experimental results of medical image fusion, the objective evaluation metrics listed are much higher than other compared meth-

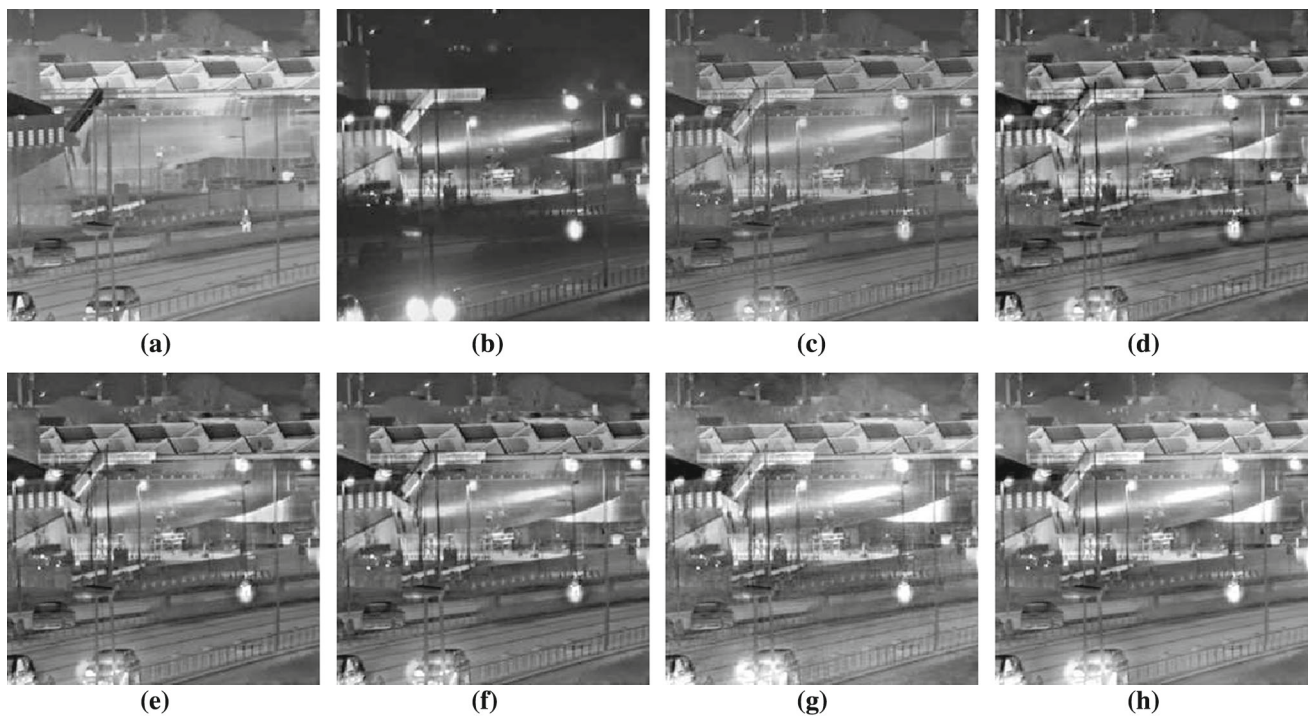


Fig. 6 Infrared and visible images and the corresponding fused images. **a** Infrared image, **b** visible image, **c** GP, **d** DWT, **e** NSCT, **f** NSST, **g** MCA, **h** NSST + MCA

Table 3 Quantitative comparison results of the fused infrared and visible images

Methods	Q_E	Q_W	Q_0	$Q^{AB/F}$	Entropy
GP	0.3653	0.7968	0.7484	0.5948	7.0532
DWT	0.3538	0.8107	0.7325	0.5837	7.2866
NSCT	0.3747	0.8312	0.7645	0.6194	7.2683
NSST	0.3841	0.8312	0.7640	0.6212	7.2655
MCA	0.3211	0.8155	0.7198	0.5263	7.4004
Proposed	0.3841	0.8348	0.7760	0.6189	7.4030

ods, which indicates that the proposed algorithm is of great potential for the fusion of medical images.

In addition, the computational complexity of the proposed method and compared methods are considered. All the experiments are implemented in MATLAB R2011b version on a PC with Core i5 3.20 GHz CPU and 3GB RAM. The average computation time of various methods for source images is given in Table 4. It can be seen that the GP method and DWT method are faster than other compared method as they have lower computational complexity. The higher computational efficiency of NSST makes it run faster than NSCT method. The MCA method and the proposed method are the most time-consuming as they include complex iterative computation. Although the proposed method spends slightly more time than MCA method, it is worthy to obtain better fusion results.

Table 4 Average computation time of compared methods

Methods	GP	DWT	NSCT	NSST	MCA	Proposed
Time (s)	0.055	0.056	66.801	1.350	472.090	487.062

5 Conclusion

In this paper, a novel image fusion algorithm based on NSST and MCA is proposed. As an excellent multi-scale geometric analysis tool, the NSST can represent the source images sparsely; therefore, the edges and geometric features can be easily fused in the high-pass subbands by the sum-modified-Laplacian scheme. With the help of morphological component analysis, detail information of low-pass subbands can be extracted and fused efficiently. More details of source images are transferred to the fused images in the proposed scheme. The experimental results on different kinds of images show that the proposed algorithm outperforms some other widely used image fusion algorithms in the visual effect and objective evaluation.

References

- Li, S., Kwok, J.T., Tsang, I.W., Wang, Y.: Fusing images with different focuses using support vector machines. *IEEE Trans. Neural Netw.* **15**(6), 1555–1561 (2004)

2. Kang, X., Li, S., Benediktsson, J.A.: Feature extraction of hyperspectral images with image fusion and recursive filtering. *IEEE Trans. Geosci. Remote Sens.* **52**(6), 3742–3752 (2014)
3. Yin, H.: Sparse representation with learned multiscale dictionary for image fusion. *Neurocomputing* **148**, 600–610 (2015)
4. Miao, Q., Shi, C., Xu, P., Yang, M., Shi, Y.: A novel algorithm of image fusion using shearlets. *Opt. Commun.* **284**(6), 1540–1547 (2011)
5. Chanussor, J., Mauris, G., Lambert, P.: Fuzzy fusion techniques for linear features detection in multitemporal SAR images. *IEEE Trans. Geosci. Remote Sens.* **37**(3), 1292–1305 (1999)
6. Jiang, Y., Wang, M.: Image fusion with morphological component analysis. *Inf. Fusion* **18**, 107–118 (2014)
7. Toet, A.: Image fusion by a ratio of low-pass pyramid. *Pattern Recognit. Lett.* **9**(4), 245–253 (1989)
8. Burt, P.T., Kolczynski, R.J.: Enhanced image capture through fusion. In: *Proceedings of the 4th International Conference on Computer Vision*, pp. 173–182, Berlin, Germany (1993)
9. Li, H., Manjunath, B.S., Mitra, S.K.: Multi-sensor image fusion using the wavelet transform. In: *Proceedings of IEEE International Conference on Image Processing*, pp. 51–55, Austin, USA (1994)
10. Wang, H.H.: A new multiwavelet-based approach to image fusion. *J. Math. Imaging Vis.* **21**(2), 177–192 (2004)
11. Lewis, J.J., OCallaghan, R.J., Nikolov, S.G., Bull, D.R., Canagarajah, N.: Pixel-region-based image fusion with complex wavelets. *Inf. Fusion* **8**(2), 119–130 (2007)
12. Qu, X., Yan, J., Xiao, H., Zhu, Z.: Image fusion algorithm based on spatial frequency-motivated pulse coupled neural networks in nonsubsampling contourlet transform domain. *Acta Autom. Sin.* **34**(12), 1508–1514 (2008)
13. Wang, J., Peng, J., Feng, X., He, G., Wu, J., Yan, K.: Image fusion with nonsubsampling contourlet transform and sparse representation. *J. Electron. Imaging* **22**(4), 043019 (2013)
14. Wang, L., Li, B., Tian, L.: Multi-modal medical image fusion using the inter-scale and intra-scale dependencies between image shift-invariant shearlet coefficients. *Inf. Fusion* **19**, 20–28 (2014)
15. Yin, M., Liu, W., Zhao, X., Yin, Y., Guo, Y.: A novel image fusion algorithm based on nonsubsampling shearlet transform. *Optik* **125**, 2274–2282 (2014)
16. Kong, W., Liu, J.: Technique for image fusion based on nonsubsampling shearlet transform and improved pulse-coupled neural network. *Opt. Eng.* **52**(1), 017001 (2013)
17. Cands, E.J., Donoho, D.L.: Ridgelets: a key to higher-dimensional intermittency? *Philos. Trans. R. Soc. Lond. A* **357**, 2495–2509 (1999)
18. Chen, T., Zhang, J., Zhang, Y.: Remote sensing image fusion based on ridgelet transform. In: *Proceedings of IEEE International Geoscience and Remote Sensing Symposium*, pp. 1150–1153 (2005)
19. Nencini, F., Garzelli, A., Baronti, S., Alparone, L.: Remote sensing image fusion using the curvelet transform. *Inf. Fusion* **8**(2), 143–156 (2007)
20. Yang, L., Guo, B.L., Ni, W.: Multimodality medical image fusion based on multiscale geometric analysis of contourlet transform. *Neurocomputing* **72**(1–3), 203–211 (2008)
21. Labate, D., Lim, W., Kutyniok, G., Weiss, G.: Sparse multidimensional representation using shearlets. In: *Proceedings of SPIE 5914, Wavelets XI*, 59140U, pp. 254–262 (2005)
22. Shi, C., Miao, Q., Xu, P.: A novel algorithm of remote sensing image fusion based on Shearlets and PCNN. *Neurocomputing* **117**(10), 47–53 (2013)
23. Easley, G., Labate, D., Lim, W.: Sparse directional image representations using the discrete shearlet transform. *Appl. Comput. Harmon. Anal.* **25**(1), 25–46 (2008)
24. Kong, W., Zhang, L., Lei, Y.: Novel fusion method for visible light and infrared images based on NSST-SF-PCNN. *Infrared Phys. Technol.* **65**, 103–112 (2014)
25. Singh, S., Gupta, D., Anand, R.S., Kumar, V.: Nonsubsampling shearlet based CT and MR medical image fusion using biologically inspired spiking neural network. *Biomed. Signal Process.* **18**, 91–101 (2015)
26. Gao, G., Xu, L., Feng, D.: Multi-focus image fusion based on nonsubsampling shearlet transform. *IET Image Process.* **7**(6), 633–639 (2013)
27. Liu, X., Zhou, Y., Wang, J.: Image fusion based on shearlet transform and regional features. *Int. J. Electron. Commun.* **68**, 471–477 (2014)
28. Kong, W.: Technique for gray-scale visual light and infrared image fusion based on non-subsampling shearlet transform. *Infrared Phys. Technol.* **63**, 110–118 (2014)
29. Starck, J.L., Elad, M., Donoho, D.L.: Redundant multiscale transforms and their application for morphological component analysis. *Adv. Imaging Electron Phys.* **132**, 287–348 (2004)
30. Sardy, S., Bruce, A.G., Tseng, P.: Block coordinate relaxation methods for nonparametric wavelet denoising. *J. Comput. Graph. Stat.* **9**(2), 361–379 (2000)
31. Huang, W., Jing, Z.L.: Evaluation of focus measures in multi-focus image fusion. *Pattern Recognit. Lett.* **28**(4), 493–500 (2007)
32. Luo, Z., Ding, S.: Image fusion algorithm based on nonsubsampling contourlet transform. *Appl. Mech. Mater.* **401–403**, 1381–1384 (2013)
33. Cao, Y., Li, S., Hu, J.: Multi-focus image fusion by nonsubsampling shearlet transform. In: *Proceedings of Sixth International Conference on Image and Graphics*, pp. 17–21, Hefei, Anhui (2011)
34. Wang, Z., Bovik, A.C.: A universal image quality index. *IEEE Signal Process. Lett.* **9**(3), 81–84 (2002)
35. Piella, G., Heijmans, H.: A new quality metric for image fusion. In: *Proceedings of IEEE International Conference on Image Processing*, pp. 173–176, Barcelona, Spain (2003)
36. Xydeas, C.S., Petrovic, V.: Objective image fusion performance measure. *Electron. Lett.* **36**(4), 308–309 (2000)